

The Effect of Interstellar Absorption on Measurements of the Baryon Acoustic Peak in the Lyman- α Forest

Yishay Vadai¹, Dovi Poznanski¹, Dalya Baron¹, Peter E. Nugent²,
and David Schlegel³

¹*School of Physics and Astronomy, Tel-Aviv University, Tel Aviv 69978, Israel*

²*Computational Cosmology Center, Lawrence Berkeley National Laboratory, 1 Cyclotron Road, Berkeley, CA 94720, USA*

³*Physics Division, Lawrence Berkeley National Laboratory, 1 Cyclotron Road, Berkeley, CA 94720, USA*

Accepted XXX. Received YYY; in original form ZZZ

ABSTRACT

In recent years, the autocorrelation of the Lyman- α forest has been used to observe the baryon acoustic peak at redshift $2 < z < 3.5$ using tens of thousands of QSO spectra from the BOSS survey. However, the interstellar medium of the Milky-Way introduces absorption lines into the spectrum of any extragalactic source. These lines, while weak and undetectable in a single BOSS spectrum, could potentially bias the cosmological signal. In order to examine this, we generate absorption line maps by stacking over a million spectra of galaxies and QSOs. We find that the systematics introduced are too small to affect the current accuracy of the baryon acoustic peak, but are comparable to the statistical noise level expected from future surveys such as the Dark Energy Spectroscopic Instrument (DESI). We outline a method to account for this with future datasets.

Key words: cosmology: observations – interstellar medium

1 INTRODUCTION

The baryon acoustic peak is cosmological feature of a predictable physical size, which can be used to constrain cosmological parameters that describe the expansion of universe. It was first discovered in the power spectrum of temperature differences in the Cosmic Microwave Background (CMB) radiation, where it is known as Baryon Acoustic Oscillations (BAO; de Bernardis et al. 2000, Keisler et al. 2011; Sievers et al. 2013; Hinshaw et al. 2013; Planck Collaboration et al. 2014). The same phenomenon can be seen as a single peak in the autocorrelation of baryon density, and it has first been observed in the autocorrelation of galaxy number counts (Eisenstein et al. 2005).

The Baryon Acoustic Oscillations Survey (BOSS) (Dawson et al. 2013) project, part of the Sloan Digital Sky Survey (SDSS; York et al. 2000), has obtained spectra for about 2.5×10^6 galaxies, and about 6×10^5 QSOs, spread over about a third of the sky. In recent years, there have been a number of works which used BOSS data to measure the baryon peak using absorption in the Lyman- α forest of QSOs at a redshift range of about $2 < z < 3.5$ (Busca et al. 2013; Slosar et al. 2013; Delubac et al. 2015).

The baryon acoustic peak is a weak feature, and the typical signal-to-noise ratio (SNR) of the forest is low. Averaging over $\sim 10^5$ QSOs is required in order to achieve the required SNR in the autocorrelation function. This makes

this process potentially sensitive to systematics that could be in the data, even if they cannot be detected in a single QSO spectrum. In this paper, we focus on one such effect, which is intervening absorption lines formed in the interstellar medium (ISM) of the Milky Way (MW). Interstellar emission (see e.g., Brandt & Draine 2012) will not be considered here.

ISM absorption at some wavelength, if not accounted for, could mimic Lyman- α at particular redshifts. If there are correlations between absorption lines, or between sight lines, they could introduce a spurious signal to the 2D autocorrelation function of the Lyman- α forest, and bias the shape or position of the baryon acoustic peak.

Poznanski et al. (2012) followed by Baron et al. (2015a,b), have used the integrated MW absorption spectrum in order to study correlations of absorption features with dust extinction, and the properties of the Diffuse Interstellar Bands (DIBs; see also Murga et al. 2015 and Lan et al. 2016). They achieved this by stacking hundreds of thousands of SDSS spectra, in which the lines are not detected individually. The SDSS coverage allowed them to probe different extinction regimes, as well as different directions on the sky. In this work we use the same methodology in order to measure the ISM features. In order to calculate the autocorrelation of Lyman- α forest, we re-created a pipeline which is similar to previous works (Busca et al. 2013; Slosar et al. 2013;

Delubac et al. 2015). Combining these two approaches, we study the ISM contribution in isolation from other effects.

Near the final stages of this work, Bautista et al. (2017) published an updated measurement of the Lyman- α BAO autocorrelation from 12th data release (DR12) of SDSS BOSS (Alam et al. 2015). There, they briefly discuss the possible systematic contribution of the MW ISM to the BAO signal, which we study here in detail.

2 BARYON PEAK PIPELINE

In order to measure the ISM contribution to the autocorrelation of the Lyman- α forest, we need a pipeline to calculate the autocorrelation estimator. We follow the method used in Busca et al. (2013), Slosar et al. (2013), and Delubac et al. (2015), with some modifications as discussed below.

2.1 Data selection

We use 176 944 QSOs from BOSS DR12 with redshift $2.1 < z < 3.5$ as selected by (Ross et al. 2012), and observed as part of the BOSS program with the upgraded SDSS spectrographs (Smee et al. 2013). This redshift range translates to a wavelength range of about 3600 Å to 5500 Å. The lower limit is set by atmospheric absorption of UV light, whereas the higher limit is set by diminishing observed QSO numbers at higher redshifts. Note that this wavelength range falls within the blue cameras of the BOSS spectrographs.

Within the spectra we discard pixels as follows. First, SDSS provides a variety of flags that are derived from the subexposures, and then propagated to the reduced stacked spectrum with both AND and OR operators. We discard all pixels that are flagged in all sub-exposures (AND masking). We use only specific OR mask flags. Out of those, the BRIGHTSKY flag is the most common, and causes the removal of 18 percent of the data. A few other flags (BADTRACE, BADFLAT, MANYBADCOLUMNS) discard up to 2 additional percent. We also mask the telluric Hg I line with a 4356 Å to 4364 Å mask. This line is flagged by the SDSS pipeline in most of the spectra, but we find some residuals in other spectra as well.

We remove Broad Absorption Lines (BALs) using the BOSS catalogue (Pâris et al. 2016, DR12Q_BAL). We mask out the following lines: C IV, O VI, NV, Si IV+O IV as well as Lyman- α , based on the supplied BAL reference frames (minimum and maximum velocities). We add a fractional safety margin of 2×10^{-3} of the wavelength to the line widths. In order to mask Damped Lyman- α Absorption systems (DLAs), we use a catalogue provided by Garnett et al. (2016). Similarly to Delubac et al. (2015), we remove regions with more than 20 percent absorption and correct the damping wings using a Lorentzian profile for Lyman- α and Lyman- β , ignoring possible metal lines from these systems.

2.2 Continuum fit

We implement a continuum fit process based on MF-PCA (see Suzuki et al. 2005; Pâris et al. 2011; Lee et al. 2012), with some minor differences in the fit process. First, we do not perform a visual inspection of all the fitted continua (except for a small fraction of objects). Lee et al. (2012) fitted

redshift correction, power-law correction and flux normalization parameters simultaneously with the PCA coefficients, using the Levenberg-Marquardt (LM) algorithm. We perform LM on power-law correction and flux normalization, with a linear least squares for the PCA coefficients in every iteration. We find that allowing the redshift to vary produces unreliable results, especially in BAL QSOs. Instead, we use redshift values based on visual inspection from the supplied BAL catalogue, whenever possible. For every QSO, we calculate a ‘goodness of fit’ value, defined as the mean of the absolute fit errors, over a wavelength range of 1216 Å to 1600 Å. We bin the QSOs according to their SNR, and discard those with the lowest goodness of fit in every bin. To account for the lack of visual inspection, we discard the worst 10 percent of the continuum fits, instead of 5 percent as done in Lee et al. (2012). Assuming the number of pairs is quadratic with QSO density, we remove about 20 percent of the pixel pairs. At the end of this stage we discard 29662 QSOs due to bad fit, 5967 QSOs in which the continuum level is comparable to the noise, and 546 QSOs in which the forest contains less than 150 valid pixels. The forest autocorrelation is computed from the remaining 140769 QSOs. This is a similar number to the total used by Delubac et al. (2015) who used DR11 while we use DR12, but we reject more QSOs.

2.3 The autocorrelation estimator

We obtain the forest transmittance, $T(z)$ for every QSO, where z is the Lyman- α equivalent redshift of the wavelength, $f(z)$ is the QSO flux and $C_q(z)$ is the predicted continuum.

$$T(z) = \frac{f(z)}{C_q(z)} \quad (1)$$

$\bar{T}(z)$ is the mean transmittance, where the average is done over all QSOs, as a function of redshift. The fractional change in transmittance, δ_F , is defined as:

$$\delta_F(z) = \frac{T(z)}{\bar{T}(z)} - 1 \quad (2)$$

The overall slope predicted by the continuum fit is not exact, especially for higher redshift QSOs, where the forest spans a wider wavelength range. We define $\delta_F(D_C(z))$ to be $\delta_F(z)$ as a function of parallel comoving distance, $D_C(z)$. We detrend $\delta_F(D_C(z))$ of forests that span more than 500 Mpc ($h_0 = 0.7$), using a weighted nonuniform boxcar filter with a window size of ± 300 Mpc. We find, by trial and error, that the window size is large enough to avoid affecting the 2D autocorrelation in a way that distorts the baryon peak.

After calculating δ_F , for all QSOs, we remove the residual bias, $\langle \delta_F(z) \rangle$, which probably stems from an imperfect continuum fit, in every redshift bin. We then calculate the autocorrelation estimator:

$$\hat{\xi}_A = \frac{\sum_{ij \in A} w_{ij} \delta_i \delta_j}{\sum_{ij \in A} w_{ij}} \quad (3)$$

where A is a bin of comoving parallel and transverse distances between pairs of pixels. The sum over i, j represents all pixel pairs with the required distances. It is worth noting in passing, that what is commonly called the autocorrelation of the Lyman- α forest is, more precisely, the covariance

of forest transmittance, as a function of the separation in comoving coordinates. To get the autocorrelation we would have to divide by the intrinsic variance of the forest, which we cannot measure due to the measurement uncertainties.

2.4 Pixel weights

We use a model for the weights given by Busca et al. (2013), based on McDonald et al. (2006). The expression for the weight of a pair of pixels is:

$$w_{ij} \propto \frac{[(1+z_i)(1+z_j)]^{\gamma/2}}{\xi_{ii}^2 \xi_{jj}^2} \quad (4)$$

Where:

$$\xi_{ii}^2 = \frac{\sigma_{\text{pipeline},i}^2}{\eta(z_i)} + \sigma_{\text{LSS}}^2(z_i) \quad ; \quad \sigma_{\text{pipeline},i}^2 = \frac{1}{\text{ivar} \cdot (C_q \bar{T})^2} \quad (5)$$

This model takes into consideration:

- The measured redshift dependence of the correlation function $(1+z)^{-\gamma}$ where $\gamma = 3.8$.
- The flux error for each point in the forest $\sigma_{\text{pipeline},i}^2$, which in turn is based on flux error (ivar).
- Variance introduced by the large scale structure σ_{LSS} .
- A scaling factor for the contribution of pipeline variance to the correlation variance η .

We use the values obtained by Busca et al. (2013) for $\sigma_{\text{LSS}}(z)$ and $\eta(z)$.

The contributions of i and j can be separated to the product $w_{ij} = w_i w_j$, so that weights can be calculated per pixel rather than for every pair:

$$w_i = (1+z_i)^{\gamma/2} \left[\frac{1}{\text{ivar} \cdot (C_q \bar{T})^2 \eta(z_i)} + \sigma_{\text{LSS}}^2(z_i) \right]^{-1} \quad (6)$$

2.5 Implementation

Our pipeline is written in Python+NumPy, with the critical path in the autocorrelation calculation written in Cython. We use the reference Python implementation, which is a bytecode interpreter, and as such it can be 2–3 orders of magnitude slower than compiled languages such as C. Each instruction has to be translated at runtime, which incurs an overhead. Numpy offers improved performance by including pre-compiled versions of common mathematical calculations, like matrix operations. However, some problems do not map efficiently to the ‘recipes’ provided by Numpy. Cython uses a simple syntax similar to python, while achieving performance that is comparable to C. Using Cython, we can write loops explicitly and control the iteration boundaries, which allows us to ignore pixel pairs that are too far away in redshift.

Given two QSOs, A and B , with forest sizes N and M , respectively, calculating their correlation contribution using matrix operations requires all $N \times M$ combinations of pixel pairs to be computed. A typical forest can have a range of $200 h^{-1} \text{ Mpc}$ to $600 h^{-1} \text{ Mpc}$, while the total range $1.95 < z < 3.5$ corresponds to $1700 h^{-1} \text{ Mpc}$. Given a point in QSO A , the matching points within $200 h^{-1} \text{ Mpc}$ in QSO B

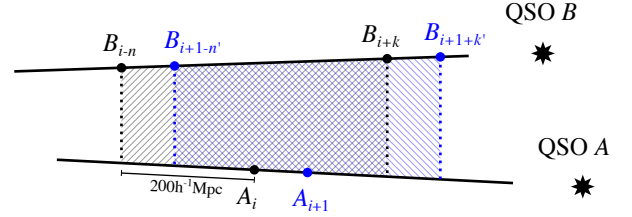


Figure 1. A diagram of two forests A, B showing how the range of relevant pixels in B for every pixel in A , is determined by the maximum correlation length of interest. When the autocorrelation length is small enough compared to a typical forest length, it is possible to avoid iterating over all pairs of forest pixels between two QSOs. The minimum (maximum) indices for each valid range form a monotonically increasing sequence. If we have a valid starting point B_{i-n} for A_i , we can begin the next iteration A_{i+1} at that point. At the other end, once at least one point in B has been found to be in range of A_i , iteration over points in B can stop if the next point is out of range.

all lie in a limited distance range. Therefore, the overlap between forests can be small, and most of the matrix elements represent points that are too far apart. Because distances are monotonically increasing, it is possible to choose the iteration boundaries of the inner loop (over QSO B) to avoid pairs which cannot be found within the required range of $200 h^{-1} \text{ Mpc}$ (see fig. 1). Suppose we know the maximal range of pixels in QSO B , $[B_{i-n}, B_{i+k}]$ that are in range of A_i . It is possible to find the maximal range $[B_{i+1-n'}, B_{i+1+k'}]$ corresponding to the next point in A , A_{i+1} , without iterating over all points in B for every A_i , because the series of range start (or end) points is monotonically increasing as well.

In order to find the set of all QSO pairs, we choose QSOs that are separated by less than $3^\circ 16'$ which corresponds to about $200 h^{-1} \text{ Mpc}$ at $z = 1.9$. The 1.5×10^5 QSOs form about 2×10^{10} potential pairs, out of which only 5×10^7 unique pairs are within the required angular range. We use a KD-Tree implementation in the *astropy* package, which can perform a k-Nearest Neighbor Search in $O(k \log n)$. To parallelize the search, each core is assigned a different subset of the QSOs, to check against the full list of QSOs.

The pipeline supports parallelization through MPI, using the *Mpi4Py* package. Performance is about 3×10^7 pixel pairs per second per core. The BOSS forest yields $\sim 3 \times 10^{12}$ pixel pairs and can be calculated within an hour on a 32-core machine.

Every pixel pair in our pipeline is binned according to sky region (HealPix bin), parallel comoving separation, transverse comoving separation, and parallel comoving distance (the average distance of the pixel pair). The range and resolution on each axis can be changed to obtain different cuts of the results (a tradeoff is required to prevent the size of the 4-dimensional array from becoming too large).

We make the pipeline source code available at:

<https://github.com/yishayv/lyacorr>.

2.6 Lyman- α autocorrelation results

Figure 2 shows the autocorrelation estimator, $\hat{\xi}$, as a function of parallel and transverse comoving separation, $(r_{\parallel}, r_{\perp})$. We include the autocorrelation estimator from Delubac et al. (2015) for comparison (received by private communication). Figure 3 shows the autocorrelation estimator multiplied by distance squared in three angular wedges where μ is the cosine of the angle of the coordinate $(r_{\parallel}, r_{\perp})$. There is faint trace of the BAO signal, at small angles, with an amplitude of about $\sim 5 \times 10^{-5}$.

Since our purpose is not to perform a full cosmological measurement, we did not derive the covariance matrix of the autocorrelation estimator, so we do not have a robust error estimation, in contrast to previous works. However, the autocorrelation estimator values are similar to previous results with the same data, with slightly more noise along r_{\perp} , appearing as faint vertical stripes in fig. 2.

3 STACKED ISM SPECTRA

Poznanski et al. (2012) have used stacked, detrended SDSS spectra to measure the correlation of dust extinction with the Na I D absorption doublet. Baron et al. (2015a,b) have expanded that process to the entire wavelength range of the SDSS spectrograph to detect multiple DIBs, study their properties and correlations among themselves and with other species.

Baron et al. (2015a) used only data redder than 3800 Å, corresponding to a Lyman- α redshift of 2.1, due to the limits of the original SDSS spectrographs (Smeed et al. 2013). We create ISM spectra using a similar process, using only spectra from the BOSS spectrograph, with a limit of 3600 Å, or a Lyman- α redshift below 2. We use all 1.5×10^6 galaxies and 5×10^5 QSOs from the 12th data release (DR12). For every spectrum, we estimate the continuum using a Savitzky-Golay filter with a 80 Å window. This is a narrower window than in the previous works, which accounts for our interest in shorter wavelengths. For every object (galaxy or QSO), we divide the original spectrum by the continuum to obtain a (noisy) detrended spectrum of relative absorption. Pixels where the continuum was nonpositive or comparable to noise (below 0.5×10^{-17} erg/s/cm²/Å) were discarded. We then calculate the median of the detrended spectra, at every wavelength, in 20 bins of extinction, using the maps of Schlegel et al. (1998). The bin boundaries are chosen so that there is a similar number of spectra in each bin.

Since, generally speaking, QSOs are blue and galaxies are red, the blue end of the median spectra is dominated by QSOs (fig. 4), and the red by galaxies, where their much larger number contributes in addition to their colour. The split point occurs at roughly 4400 Å which corresponds to a redshift of ~ 2.6 . The Lyman- α autocorrelation data spans $2 < z < 3.5$, but most of the statistical weight is near $z \sim 2.2$. This means that for the most part, our ISM estimation relies on the $\sim 5 \times 10^5$ QSO spectra, which include the Lyman- α QSOs and lower redshift QSOs, and we cannot leverage significantly the power in the galaxy spectra. Lyman- α QSOs account for about half of the total flux in the u and g bands.

The stacked ISM spectra are shown in fig. 5. Each row represents a spectrum in a single extinction bin. The mean

absorption has been removed to show only features that are correlated with extinction. One can see that the spectra are very noisy at short wavelengths, where there is a penury of photons, and that only very strong lines appear. The Ca II H&K lines (3968 Å and 3933 Å) are clearly the most notable feature in our range. There may be a trace of O II lines at 3727 Å and 3729 Å. The artifact at ~ 5580 Å is caused by the transition between the red and blue spectrographs. The Na I doublet can be seen near 5890 Å. Also visible are the DIBs at 5780 Å and, to a lesser extent, 5797 Å.

4 ESTIMATING THE ISM INFLUENCE ON THE BAO SIGNAL

We proceed to estimate the influence of the ISM absorption lines on the baryonic peak. We identify two potential ways for the ISM to produce a BAO like feature in the autocorrelation function: The first is correlation between different lines at different wavelengths. Such correlations would mimic intrinsic Lyman- α correlations in the parallel direction, along the line of sight, and have no angular dependence. Additionally, there could be angular correlations in all (or some) of the line strengths, due to preferred scales in the MW gas distribution.

4.1 Wavelength/parallel component

For correlations between lines to bias the BAO measurement, lines would need to have wavelength separations that correspond to a comoving distance of the same order as the baryon peak. The spurious feature created by such lines would be at a comoving distance that is the mean of the apparent comoving distance of the lines (when wrongly interpreted as Lyman- α).

To create a BAO-like signal of the same strength ($\sim 5 \times 10^{-5}$) using absorption line pairs, we would need relative absorption which is the square root of the signal strength, $\sim 7 \times 10^{-3}$, for a particular redshift value. However, because we average over a large redshift range, multiple lines would have to conspire to create a single feature that would not be smoothed.

Consider absorption lines with an effective profile $\Delta\lambda_1, \Delta\lambda_2$ and average relative absorption f_1, f_2 , over a redshift range $\Delta\lambda_{\text{survey}}$. For simplicity, we treat the measured absorption profile as a boxcar function. In addition, for simplicity, we disregard the nonlinear relation between wavelength/redshift and comoving distance.

Assuming the correlation function resolves the lines (in comoving space), their contribution (without taking noise into account) would be:

$$f_1 f_2 \frac{\Delta\lambda_1 \Delta\lambda_2}{(\Delta\lambda_{\text{survey}})^2}. \quad (7)$$

The effect is attenuated by the fact that we measure forest absorption relative to the mean transmittance over the whole survey. On the other hand, the statistical weight contribution varies with redshift. Therefore, it would be wise to take a smaller, more conservative estimate for $\Delta\lambda_{\text{survey}}$. For BOSS, most of the data is around redshift 2.1 to 2.5, so the wavelength range is about 500 Å.

For the strongest lines in our redshift of interest, the

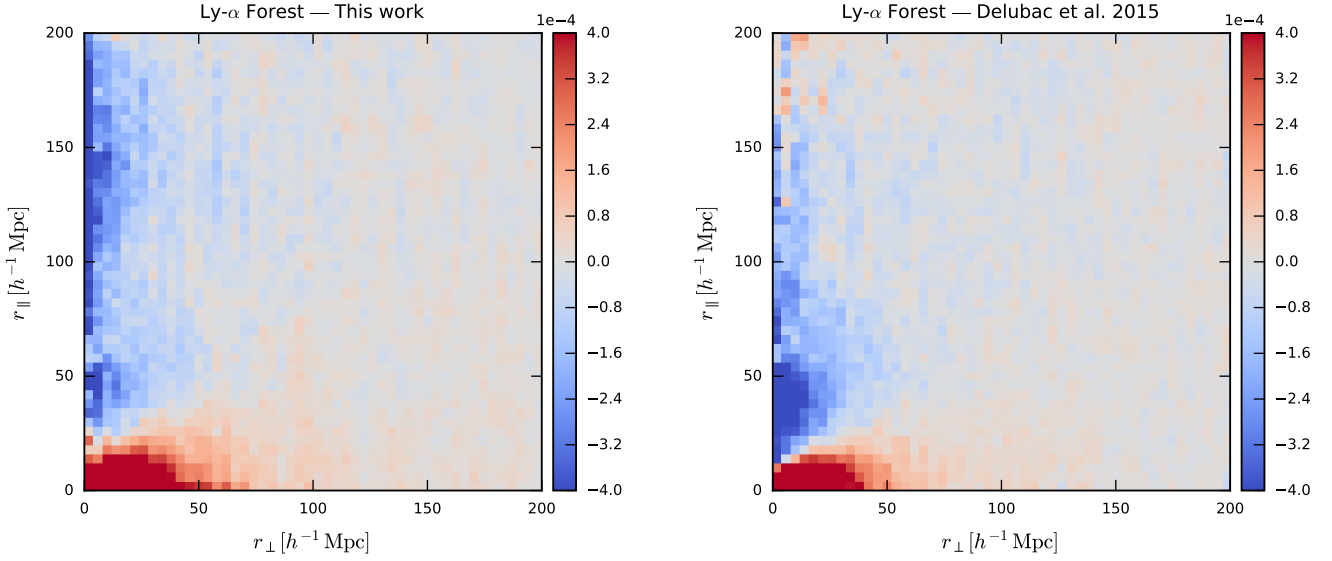


Figure 2. Autocorrelation, $\hat{\xi}_A$, of the change in transmittance δ_F , in comoving distance bins in parallel and transverse directions. The baryon peak should have the form of a quarter circle around the origin with a radius of $\sim 100 h^{-1} \text{ Mpc}$. In addition to a faint trace of the BAO signal, one can see a strong peak near the origin, due to the large scale structure, as well as spurious anticorrelation at short perpendicular distances due to redshift distortion (Kaiser 1987; Tian et al. 2011). Left: This work. Right: Data from Delubac et al. (2015).

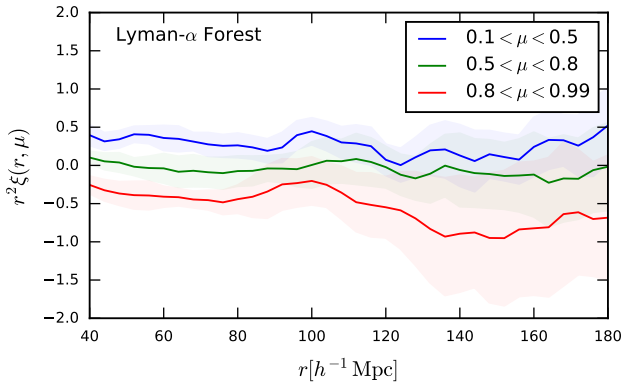


Figure 3. Lyman- α Autocorrelation, $\hat{\xi}$, multiplied by distance squared in three angle ranges where μ is the cosine of the angle of the coordinate (r_{\parallel}, r_{\perp}). We expect to see the acoustic peak at $\sim 100 h^{-1} \text{ Mpc}$. Such a peak is only notable (if barely) at the smallest angles, similarly to the results of Delubac et al. (2015). Note the plotted autocorrelation and uncertainty do not take into account the covariance of the correlation bins.

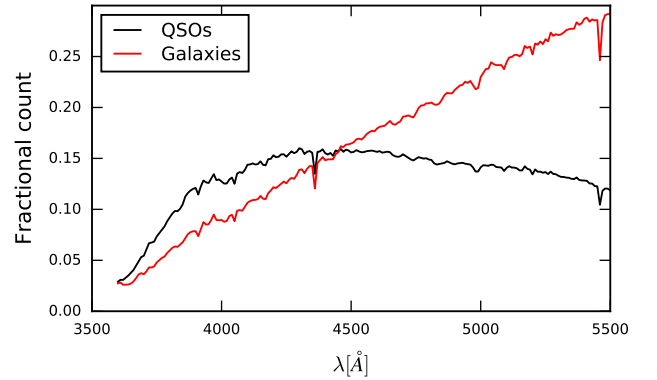


Figure 4. Contribution of galaxies vs. QSOs to the ISM spectra. The plot shows the fraction of objects with relative absorption in the range 0.9 to 1.1. The median is almost always within this range, so the density of objects determines the amount of statistical noise. At wavelengths shorter than $\sim 4400 \text{ \AA}$ the median value is determined mostly by QSOs.

Ca II H&K, we find in the stacked ISM spectra a relative absorption of 10 percent, but less than 3 percent change in absorption between the highest and lowest extinction bins. Using a ballpark value of 5 percent, we obtain:

$$0.05^2 \frac{(5 \text{ \AA})^2}{(500 \text{ \AA})^2} = 2.5 \times 10^{-6} \quad (8)$$

This number, despite rather extreme choices is still 20 times smaller than the BAO amplitude of $\sim 5 \times 10^{-5}$.

We estimated the effect of this perturbation on the apparent baryon peak position by approximating both the baryon peak and a Ca II H&K-induced bias as Gaussian curves. We fitted a Gaussian curve to the sum of the signals to find the displacement in the primary peak position. The maximum displacement is of order 0.3 percent, when the line is positioned at $\sim 0.7 \sigma$ from the primary peak. Specifically for the Ca II H&K line, the maximum displacement is in the

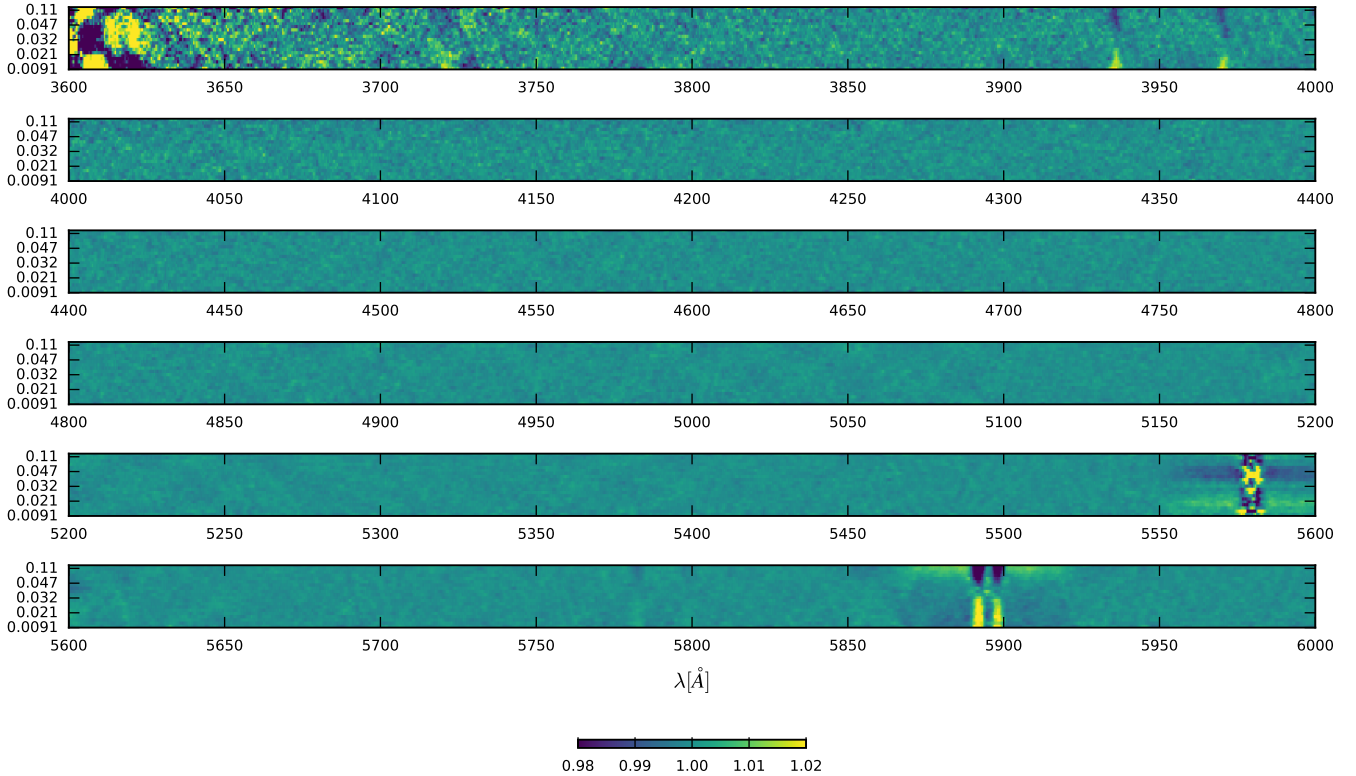


Figure 5. Stacked ISM spectra from BOSS galaxies and QSOs, in bins of extinction. The bin boundaries are chosen so that there is a similar number of spectra in each bin. The mean absorption at each redshift has been removed to show only how absorption correlates with extinction. Our range of interest is 3600 Å to 5500 Å (Lyman- α redshift of 1.95 to 3.5). The blue extreme is noisy so we cannot say much about it (it also has small contribution to the Lyman- α autocorrelation due to the weighting scheme). The Ca II H&K lines (3968 Å and 3933 Å) are clearly the most notable feature in our range. There may be a trace of O II lines at 3727 Å and 3729 Å. The artifact at ~ 5580 Å is caused by the transition between the red and blue spectrographs. The Na I doublet can be seen at 5890 Å and 5896 Å. Also visible are the DIBs at 5780 Å and, to a lesser extent, 5797 Å. In order to show small changes in intensity, we chose a colour scale that saturates some of the data.

$0.1 < \mu < 0.5$ angular wedge. However, the exact bias this could introduce depends on the details, mainly the location of this spurious peak, and to a certain extent the fit method, but it is marginally significant for BOSS QSOs.

4.2 Angular component

Most of the statistical weight in BOSS data occurs around $z = 2.2$. This can be seen in figs. 6 and 7, where we calculate the relative contribution at different redshifts to the autocorrelation function. The baryon peak scale of $100 h^{-1}$ Mpc corresponds to about 1.5° at this redshift. As a consequence of the rather narrow peak, using different redshifts might not be enough to completely erase transverse correlations that may exist at the $\sim 1^\circ$ scale in the ISM. As discussed above, the sky density of galaxies and QSOs in SDSS is insufficient to quantify these, if they exist. Instead, we can again use extinction maps as a proxy to ISM absorption lines.

We calculate the angular autocorrelation of extinction in two ways: In Method 1, we use the foreground extinction through every QSO sightline using the maps of Schlegel et al. (1998). We compute the autocorrelation in angular bins for all possible pairing within a maximum separation of $\sim 3^\circ$.

The resulting angular autocorrelation can be seen in fig. 8. Clearly, there is no preferred scale, as also shown in Figure 9 of Schlegel et al. (1998).

In Method 2, we use the extinction map from the Planck collaboration (Planck Collaboration et al. 2016). We calculate the angular autocorrelation for different regions of the sky, within the SDSS field. The result, as seen in fig. 9 is effectively identical. While extinction varies greatly in magnitude at different galactic latitudes, the autocorrelation function in all fields has a smooth slope which decreases with angular separation. It appears there is no preferred scale in the dust column density. This entails that, to first order, we do not expect any significant transverse spurious correlation from the ISM.

4.3 Autocorrelation of stacked ISM spectra

Since the correlation computation is multi-staged, complex, and very non-linear, we proceed with a data driven approach to quantifying the ISM absorption effect on the autocorrelation estimator. Optimally we would want to derive an ISM spectrum along every sightline, however, since most of our signal in the blue is from QSOs, the source density in BOSS

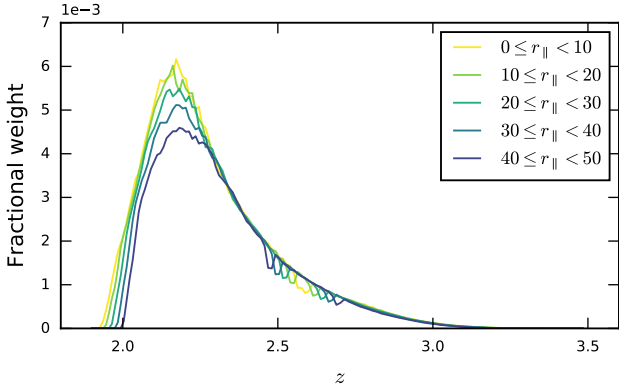


Figure 6. Weights of pixel pairs in the autocorrelation function, in slices of redshift, binned by their parallel separation r_{\parallel} . The low redshift end of the forest contributes only to low separation bins, creating a selection effect. The dips around $z \sim 2.6$ are a result of masking the telluric Hg I line.

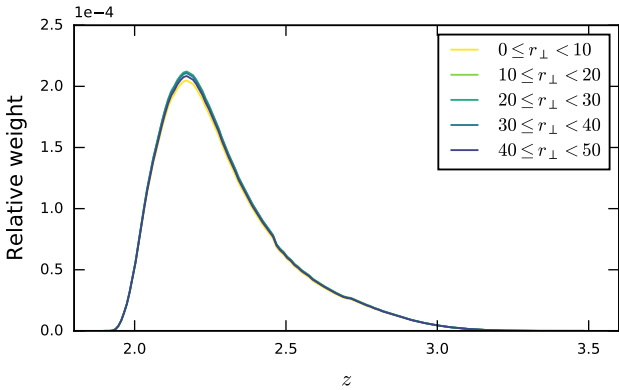


Figure 7. Weights of pixel pairs in the autocorrelation function, in slices of redshift, binned by their transverse separation r_{\perp} . Because the number of pairs scales linearly with the transverse separation, we divided the average scale from each bin. It is clear to see there is very little dependence on the transverse separation, even at high redshifts where the density of QSOs is the smallest.

is insufficient. Instead, since to first order all the absorption lines correlate with extinction, we can make a reasonable estimate of the effect of ISM absorption, by using extinction as a proxy for line strength.

For every QSO sightline we use the dust extinction (from the maps of [Schlegel et al. 1998](#)) to substitute the actual spectrum and Lyman- α forest with a stacked ISM spectrum. The Baryon Peak pipeline then proceeds normally, removes the mean transmittance as before, and only features that are correlated with extinction remain.

We then proceed to compute the autocorrelation function in bins of comoving separation. We discard pixels pairs with $z < 2.1$ because the ISM spectra are dominated by noise in this range. We plot the ISM autocorrelation estimator in a similar way to the Lyman- α forest, in figs. 10 and 11. From this calculation we find the following. First, the amplitude of the signal from the ISM is at most lower by two orders of magnitude compared to the cosmological component. Sec-

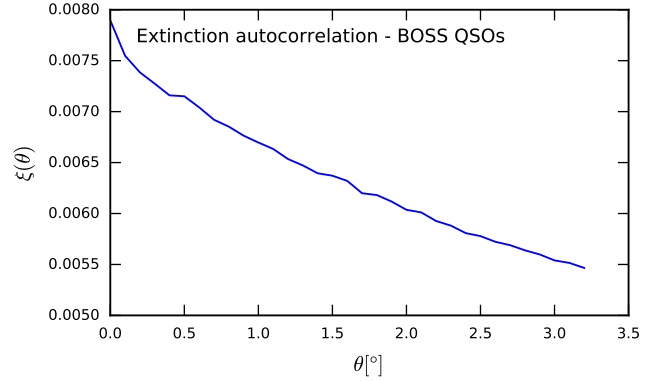


Figure 8. Autocorrelation of extinction as a function of the angle of separation θ . Produced using the extinction values from SDSS for every QSO, summed over all pairs of QSOs. The SDSS extinction value is derived from the SFD maps ([Schlegel et al. 1998](#)).

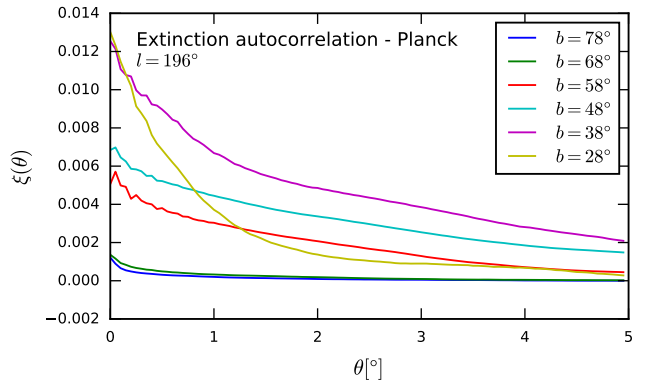


Figure 9. Same as Figure 8, but produced using extinction maps from [Planck Collaboration et al. \(2016\)](#). The various curves show the autocorrelation inside circular discs ($r = 10^\circ$) at different galactic latitudes.

ondly, since we see horizontal stripes with no angular dependence, we conclude that the correlation caused by the ISM is independent of angular separation, or transverse comoving distance. The stripes that are seen are at least partly due to detrending artifacts or noise in our stacked ISM spectra. This can still, however, serve as a rough upper bound on the magnitude and orientation of whatever effect the ISM might introduce. This is consistent with our less direct analysis in sections 4.1 and 4.2.

4.4 Autocorrelation in distance bins

In order to study the effect of specific lines, most notably Ca II H&K, we divided the data into bins of parallel comoving distance (effectively redshift or wavelength bins).

Figure 12 shows how the Ca II H&K lines create spurious correlations with each other as well as with other weaker features in the ISM spectrum. The total correlation contribution of the Ca II H&K peaks, weighted according to its corresponding redshift bin, is about 6×10^{-6} , comparable

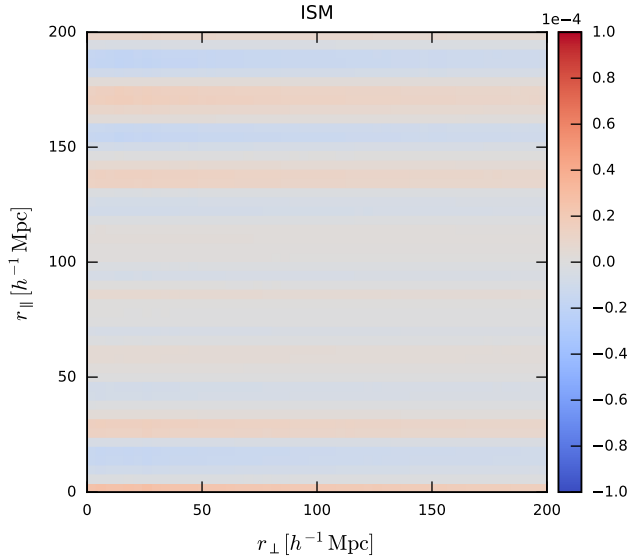


Figure 10. ISM Autocorrelation ξ_A of the change in transmittance δ_F , in comoving distance bins in parallel and transverse directions. Note that the colour range is different and much smaller than in fig. 2. Clearly any correlation the ISM might introduce is much smaller than the cosmological signal.

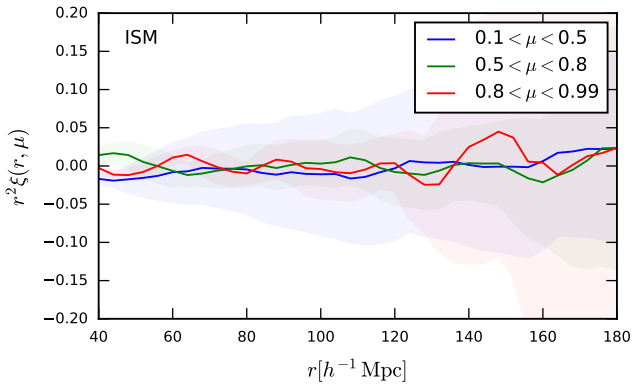


Figure 11. ISM Autocorrelation multiplied by distance squared in three angle ranges where μ is the cosine of the angle of the coordinate $(r_{\parallel}, r_{\perp})$. Since correlation between ISM absorption lines does not depend on line of sight, their contribution is smoothed in the transverse wedge. Note the different scales on the Y-axis compared with fig. 3.

to our estimate in section 4.2, and an order of magnitude smaller than the BAO signal. We find that the largest impact is from the Ca II H&K lines, and can be treated as an upper limit for the impact of the ISM on the autocorrelation.

5 IMPACT ON FUTURE SURVEYS

While we find that the ISM has a negligible impact on the cosmological signal recovered from BOSS QSOs, we would

like to quantify whether future surveys, such as the Dark Energy Spectroscopic Instrument (DESI), need to take this contaminant into consideration. DESI will obtain spectra with a resolving power similar to that of BOSS, with a comparable SNR for fainter QSOs observed with the larger telescope (DESI Collaboration et al. 2016), and that the SNR of individual spectra is similar as well.

We use the QSO density estimate from the DESI final design report (DESI Collaboration 2016, Table 2.7) to simulate a random Lyman- α forest which resembles what we expect from DESI, but without any large scale correlations. We choose forests from random SDSS QSOs with a survey area of about 10000 deg^2 . This value lies between the proposed descoped DESI survey (9000 deg^2) and the full DESI survey (14000 deg^2).

We begin by taking the expected DESI QSO density as a function of redshift and using it as a probability distribution function (PDF). We smooth the PDF using linear interpolation. We draw 672 000 z values using the smoothed PDF, and match every value with an SDSS QSO of a similar redshift. We take the pre-calculated $\delta_F(z)$ values of every SDSS QSO forest, and rescale them to the chosen z value. Since most SDSS forests will appear more than once in our sample, we multiply every selected forest by a random sign, to avoid contaminating the autocorrelation function with positive contribution from same-forest pairs. We then draw another random SDSS QSO, and use its sky position, with a small random displacement as the position of our new artificial DESI forest. We then compute the autocorrelation function of the new collection of forests.

While the large scale structure is removed by the randomization process, the resulting autocorrelation bins contain statistical noise which is similar to what we expect from the real DESI survey, under the assumption that the distributions of SNR and instrumental uncertainty values in the forest are not too different. We also obtain the accumulated statistical weight as a function of separation and redshift.

The total number of pixels summed and the total statistical weight are both about 10 times larger than in BOSS. The standard deviation of individual autocorrelation bins is $\sim 5 \times 10^{-6}$, which is the same order of magnitude of the Ca II H&K lines. In the near-parallel angular wedge, where a few bins are summed together, the Ca II H&K lines might have a noticeable contribution, but this happens at a separation much smaller than the baryon acoustic peak.

One method to treat this bias in future surveys would be to empirically derive the ISM spectrum around every QSO, by stacking nearby lower- z spectra in the observer frame, and removing the ISM contribution from every sightline. As a consequence, Lyman- α cosmology would indirectly benefit from a large density of other unrelated sources.

6 CONCLUSIONS

By building an independent (though similar) pipeline we reproduce the detection of the BAO signal in the Lyman- α forest of BOSS QSOs. We analyse in different ways the possible biases that this measurement may suffer from do to interloping lines from the MW ISM. The spurious signal could be produced by correlations between lines, i.e., in the paral-

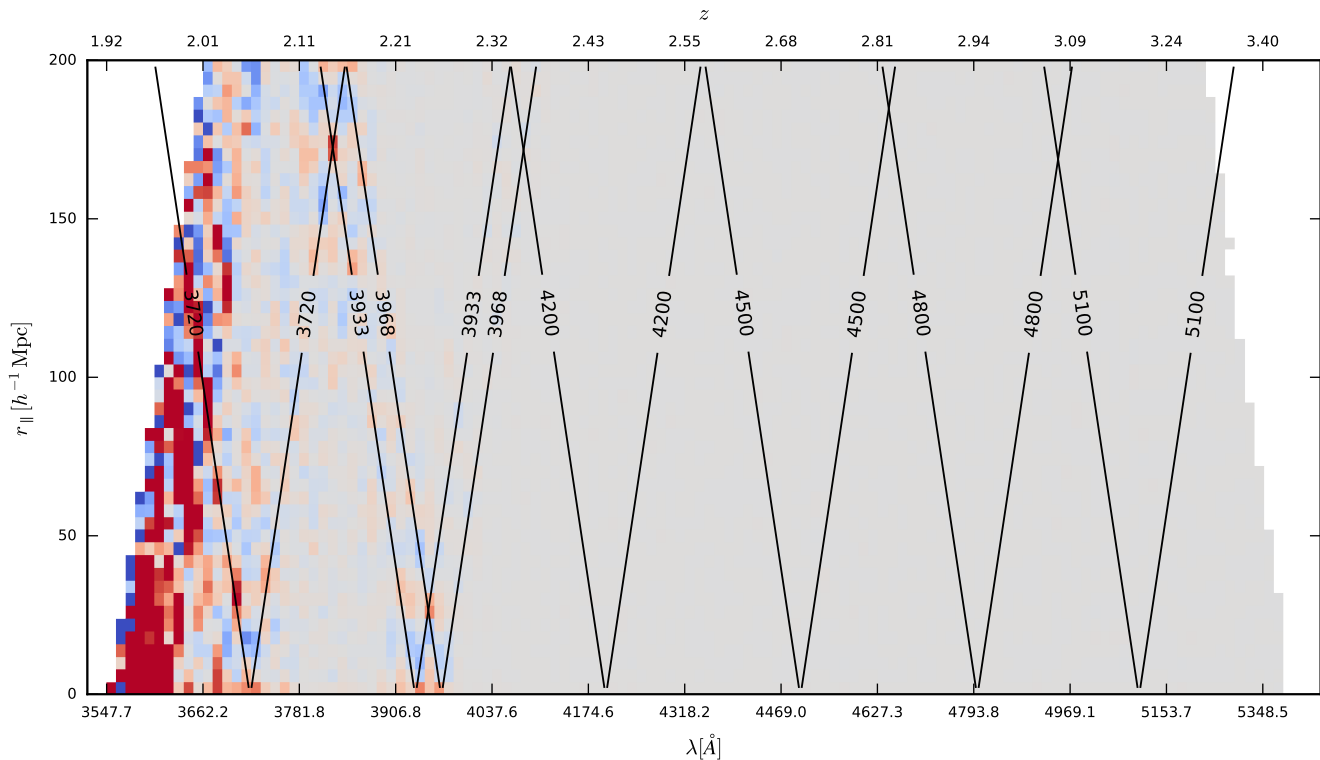


Figure 12. Autocorrelation of ISM spectra as a function of (apparent) parallel comoving separation. We use BOSS QSO sightlines where every QSO’s forest was replaced with estimated ISM absorption based on the QSO’s extinction. Each pixel comprises contribution from two different wavelengths. Each V-shaped curve shows the contribution of a single wavelength. Note the peak at the intersection of the two Ca II H&K lines (3968 Å and 3933 Å). The blue extreme, including the apparent feature at ~ 3720 Å, is noisy so we cannot say much about it (it also has small contribution to the Lyman- α autocorrelation due to the weighting scheme). The colour scale is $\pm 4 \times 10^{-4}$ which is comparable to the scale of the baryon peak, but features that affect a single distance slice are reduced by averaging over all distance slices.

lel direction, or by angular correlations on the sky, affecting the perpendicular direction.

We find that the imprint of ISM absorption is too small to significantly affect current BAO results from the 3-D Lyman- α forest. As future surveys such as DESI contain more data with more precision in BAO, it will likely be necessary to explicitly correct for these effects.

While our current analysis suffers from a lack of signal in the blue wavelength range of interest, these future surveys should have a better handle on the ISM, allowing them, via the methods presented here, to better measure and correct for biases due to the MW ISM.

ACKNOWLEDGEMENTS

We would like to thank Roman Garnett for providing us early access to the DLA catalogue from [Garnett et al. \(2016\)](#). Thanks are due to Julien Guy for his advice and for making numerical autocorrelation results available to us for comparison. This research was supported by Grant No. 2014413 from the United States-Israel Binational Science Foundation (BSF). Funding for SDSS-III has been provided by the Alfred P. Sloan Foundation, the Participating Institutions, the National Science Foundation, and the U.S. Department of Energy Office of Science. The SDSS-III web site is www.sdss3.org.

SDSS-III is managed by the Astrophysical Research Consortium for the Participating Institutions of the SDSS-III Collaboration including the University of Arizona, the Brazilian Participation Group, Brookhaven National Laboratory, Carnegie Mellon University, University of Florida, the French Participation Group, the German Participation Group, Harvard University, the Instituto de Astrofísica de Canarias, the Michigan State/Notre Dame/JINA Participation Group, Johns Hopkins University, Lawrence Berkeley National Laboratory, Max Planck Institute for Astrophysics, Max Planck Institute for Extraterrestrial Physics, New Mexico State University, New York University, Ohio State University, Pennsylvania State University, University of Portsmouth, Princeton University, the Spanish Participation Group, University of Tokyo, University of Utah, Vanderbilt University, University of Virginia, University of Washington, and Yale University.

References

- Alam S., et al., 2015, [ApJS](#), **219**, 12
- Baron D., Poznanski D., Watson D., Yao Y., Prochaska J. X., 2015a, [MNRAS](#), **447**, 545
- Baron D., Poznanski D., Watson D., Yao Y., Cox N. L. J., Prochaska J. X., 2015b, [MNRAS](#), **451**, 332
- Bautista J. E., et al., 2017, preprint, ([arXiv:1702.00176](#))

- Brandt T. D., Draine B. T., 2012, *ApJ*, **744**, 129
- Busca N. G., et al., 2013, *A&A*, **552**, A96
- DESI Collaboration 2016, DESI Final Design Report Part I: Science, Targeting, and Survey Design, <http://desi.lbl.gov/wp-content/uploads/2014/04/fdr-science-biblatex.pdf>
- DESI Collaboration et al., 2016, preprint, ([arXiv:1611.00036](https://arxiv.org/abs/1611.00036))
- Dawson K. S., et al., 2013, *AJ*, **145**, 10
- Delubac T., et al., 2015, *A&A*, **574**, A59
- Eisenstein D. J., et al., 2005, *ApJ*, **633**, 560
- Garnett R., Ho S., Bird S., Schneider J., 2016, preprint, ([arXiv:1605.04460](https://arxiv.org/abs/1605.04460))
- Hinshaw G., et al., 2013, *ApJS*, **208**, 19
- Kaiser N., 1987, *MNRAS*, **227**, 1
- Keisler R., et al., 2011, *The Astrophysical Journal*, **743**, 28
- Lan T.-W., Ménard B., Mo H., 2016, *MNRAS*, **459**, 3998
- Lee K.-G., Suzuki N., Spergel D. N., 2012, *The Astronomical Journal*, **143**, 51
- McDonald P., et al., 2006, *ApJS*, **163**, 80
- Murga M., Zhu G., Ménard B., Lan T.-W., 2015, *MNRAS*, **452**, 511
- Pâris I., et al., 2011, *A&A*, **530**, A50
- Pâris I., et al., 2016, preprint, ([arXiv:1608.06483](https://arxiv.org/abs/1608.06483))
- Planck Collaboration et al., 2014, *A&A*, **571**, A16
- Planck Collaboration et al., 2016, *A&A*, **586**, A132
- Poznanski D., Prochaska J. X., Bloom J. S., 2012, *MNRAS*, **426**, 1465
- Ross N. P., et al., 2012, *ApJS*, **199**, 3
- Schlegel D. J., Finkbeiner D. P., Davis M., 1998, *ApJ*, **500**, 525
- Sievers J. L., et al., 2013, *Journal of Cosmology and Astroparticle Physics*, **2013**, 060
- Slosar A., et al., 2013, *Journal of Cosmology and Astroparticle Physics*, **2013**, 026
- Smee S. A., et al., 2013, *AJ*, **146**, 32
- Suzuki N., Tytler D., Kirkman D., O’Meara J. M., Lubin D., 2005, *The Astrophysical Journal*, **618**, 592
- Tian H. J., Neyrinck M. C., Budavári T., Szalay A. S., 2011, *ApJ*, **728**, 34
- York D. G., et al., 2000, *AJ*, **120**, 1579
- de Bernardis P., et al., 2000, *Nature*, **404**, 955

This paper has been typeset from a \TeX / \LaTeX file prepared by the author.